arXiv:nucl-th/9812038v2  16 Dec 1998

# MARS Code Developments[*]

N. V. Mokhov, S. I. Striganov[†] and A. Van Ginneken

*Fermi National Accelerator Laboratory, P.O. Box 500, Batavia, IL 60510*

[†] *Now at Institute for High-Energy Physics, Protvino, Moscow Region, Russia*

S. G. Mashnik and A. J. Sierk

*Los Alamos National Laboratory, T-2, MS-B243, Los Alamos, NM 87545*

J. Ranft

*University of Siegen, Siegen, D-57068, Germany*

### Abstract

Recent developments in the physical model of 1 MeV to 100 TeV hadron and lepton interactions with nuclei and atoms are described. These include a new nuclear cross section library, a model for soft pion production, the cascade-exciton model, the dual parton model, deuteron-nucleus and neutrino-nucleus interaction models, detailed description of $\mu^-$, $\pi^-$ and $\overline{p}$ absorption and a unified treatment of muon and charged hadron electromagnetic interactions with matter. New algorithms are implemented into the MARS13(98) Monte Carlo code and benchmarked against experimental data. The code capabilities to simulate cascades and generate a variety of results in complex media have been also enhanced.

## 1 Introduction

The MARS Monte Carlo code system, being developed over 24 years, allows fast and reliable inclusive simulation of three-dimensional hadronic and electromagnetic cascades in shielding, accelerator and detector components in the energy range from a fraction of an electron-volt up to about 100 TeV [1]. The reliable performance of the MARS13 code [2, 3] has been demonstrated in numerous applications at Fermilab, CERN, KEK and other centers as well as in special benchmarking studies [4, 5, 6]. Recently, challenging applications at Fermilab have induced further significant developments of the code's physical model and its scoring capabilities. New developments in both the electromagnetic and strong interaction sectors as well as other enhancements to the current version – MARS13(98) [1] – are briefly described in this paper.

## 2 Nuclear Cross Sections

**Hadron-nucleon cross sections.** New compilations and parameterizations of elastic and inelastic $\sigma_{hN}$ are implemented covering a hadron kinetic energy range 1 MeV<E<100 TeV. Total cross sections,

$\sigma_{tot}$, from 1 MeV to 10 GeV for $p, n, \pi^+$ and $\pi^-$ are as predicted by the new improved algorithm [7] of the Cascade-Exciton Model (CEM) [8] code CEM95 [9] while for $K^+$, $K^-$ and $\overline{p}$ data compilations are used [10]. Parameterizations from [10] are relied upon for all particles between 10 GeV and 100 TeV. Elastic cross sections, $\sigma_{el}$, from 10 MeV to 10 GeV for $p, n, \pi^+$ and $\pi^-$ are likewise from [7] with interpolation of data [10] for $K^+$, $K^-$ and $\overline{p}$. Parameterizations from [11] are used between 10 and 200 GeV. For energies 200 GeV<E<100 TeV, the optical theorem with 'universal slope' [12] is applied. Fig. 1(a) shows comparison of data and MARS results on $\sigma_{tot}$ and $\sigma_{el}$ for $\pi^- p$ collisions.

**Hadron-nucleus cross sections.** New compilations, parameterizations and integration algorithms for total, inelastic, production and elastic $\sigma_{hA}$ are introduced into the code. Total, inelastic and elastic cross sections from 1 MeV to 5 GeV are described using new compilations and improved interpolation algorithms [13, 14]. At higher energies (5 GeV<E<100 TeV), $\sigma_{tot}$, $\sigma_{in}$, $\sigma_{prod}$ and $\sigma_{el}$ are calculated in the framework of the Glauber multiple scattering theory with the above $\sigma_{hN}$ as an input. The nucleon density distribution in nuclei is represented as the symmetrized Fermi function with the parameters of [15] for medium and heavy nuclei ($Z > 10$) and the ones of [16] for $Z < 10$. An example is shown in Fig. 1(b) for neutron-nucleus $\sigma_{tot}$ as calculated with this algorithm (solid line) and with the improved algorithm [14] (dashed line).

**Photon-nucleus cross sections.** Data compilation and interpolation algorithm for $\sigma_{\gamma N}$ with phenomenological $A$-dependence for $\sigma_{\gamma A}$ are as described in [17].

## 3  Nuclear Reactions from 10 MeV to 100 TeV

**Improved description of hadron-nucleus elastic scattering.** Two algorithms are implemented into MARS to better describe hadron-nucleus elastic scattering for 10 MeV<E<5 GeV: one from the code LAHET [18] while the other is based on a phenomenological formula [19]. As one can see from Fig. 2(a), more work is still needed here. However, at higher energies, the model used in MARS for both coherent and
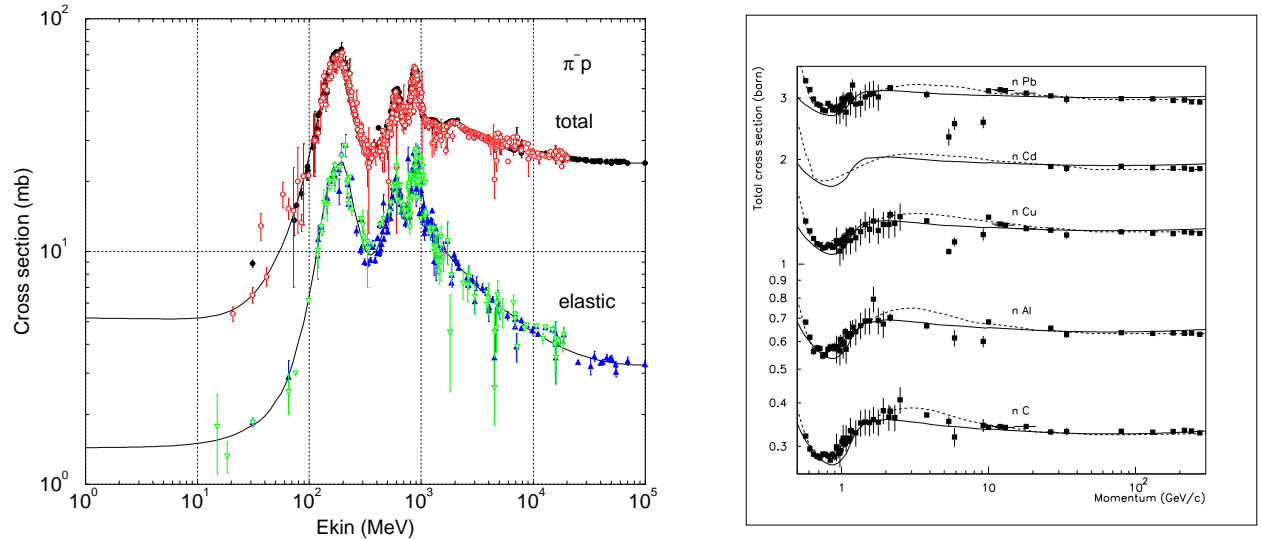


Figure 1. MARS cross sections in comparison with experimental data: (a) $\sigma_{tot}$ and $\sigma_{el}$ for $\pi^- p$ collisions as a function of pion kinetic energy; (b) $\sigma_{tot}$ for neutrons *vs* beam momentum.
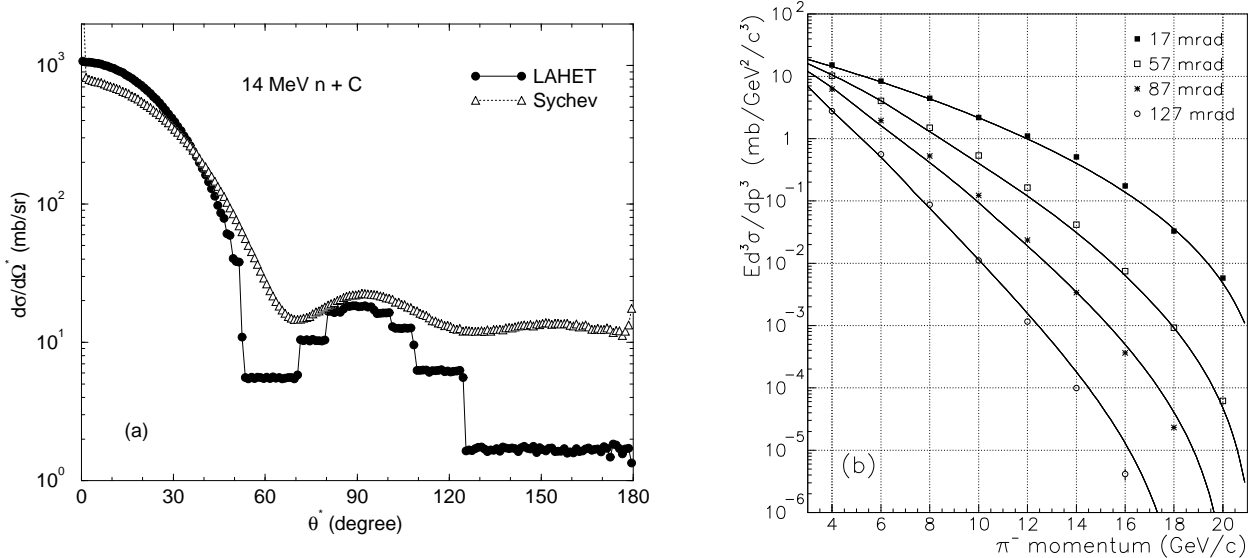
Figure 2. (a) Angular distribution of 14 MeV neutrons in center-of-mass, scattered off carbon as calculated according to LAHET [18] and [19]; (b) Pion spectra for $pp \rightarrow \pi^- X$ at four angles for proton momentum of $p_0$=24 GeV/c, data from [21].

incoherent components of $d\sigma/dt$ is quite consistent with experiment.

**New model for $\pi$-production from 5 GeV to 100 TeV.** A new phenomenological model has been developed and introduced into MARS as the default to describe pion production in high-energy proton-nucleus interactions [20]. Special attention is paid to low-momentum pions (p<2 GeV/c) from intermediate incident proton momenta (5< $p_0$ <30 GeV/c). The following form is used for the double differential cross section of the $pA \rightarrow \pi^{\pm} X$ reaction:

$$\frac{d^2\sigma^{pA \rightarrow \pi^{\pm} X}}{dp d\Omega} = R^{pA \rightarrow \pi^{\pm} X}(A, p_0, p, p_{\perp})\frac{d^2\sigma^{pp \rightarrow \pi^{\pm} X}}{dp d\Omega}, \qquad (1)$$

where $p$ and $p_{\perp}$ are total and transverse momenta of $\pi^{\pm}$, and $A$ is the atomic mass of the target nucleus. The function $R^{pA \rightarrow \pi^{\pm} X}$, measurable with much higher precision than the absolute yields, is almost independent of $p_{\perp}$ and its dependence on $p_0$ and $p$ is much weaker than for the differential cross-section itself. Rather sophisticated algorithms have been developed to treat this function for pion production on nuclei in the forward ($x_F$ >0) and backward ($x_F$ <0) hemispheres separately. It is demonstrated in [20] that model predictions are in a good agreement with data in the entire kinematic region. Typical examples of comparison with data are shown in Figs. 2(b) and 3. Calculations with the MARS13(98) code of the pion double differential spectra from a thick lead target at $p_0$=8 GeV/c agree reasonably well with data [22] in the *difficult* momentum region 0.5< $p$ <5 GeV/c (see Fig. 3(b)) whereas GEANT seems to have a problem.

**Cascade-exciton model code CEM95.** A version of the Cascade-Exciton Model of nuclear reactions [8] as realized in the code CEM95 [9] and containing also several recent refinements [7] is now implemented as default for 1-10 MeV < E < 3-5 GeV. The 1994 *International Code Comparison for Intermediate Energy Nuclear Data* has shown that CEM95 adequately describes nuclear reactions at intermediate energies and has one of the best predictive powers for double differential cross sections of secondary particles as compared to other available models. Besides that, it adds to MARS reliable $\pi^-$-capture description (with a few modifications, e.g., radiative capture $\pi^- p \rightarrow n\gamma$), better description of photon induced reactions in the
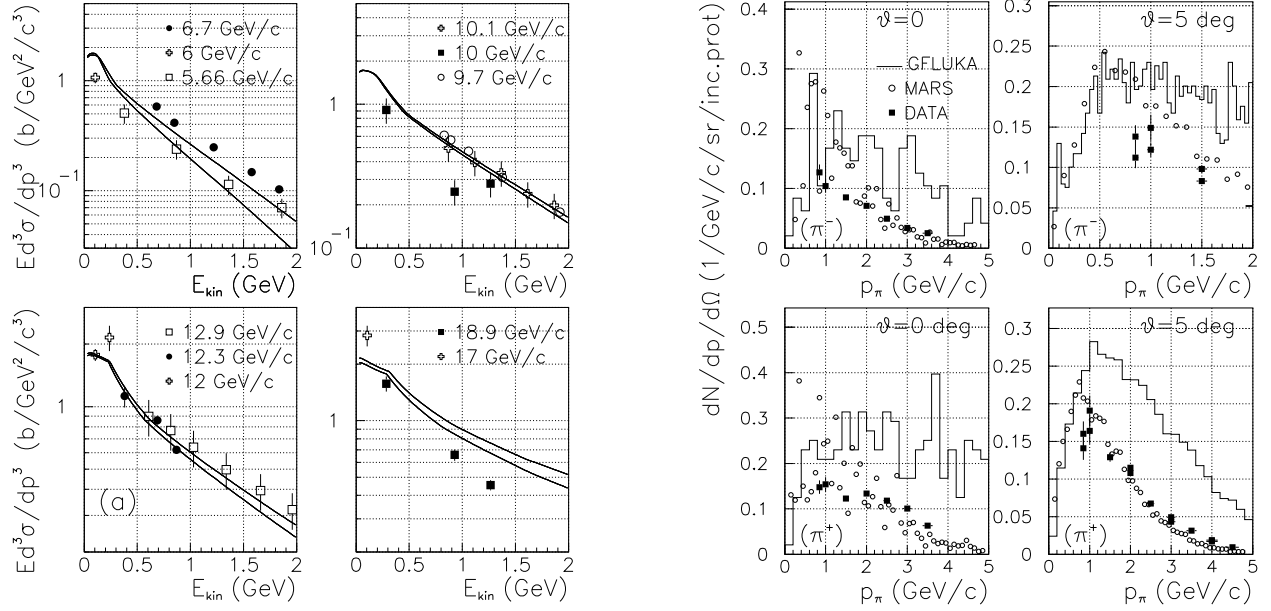
Figure 3. MARS pion spectra *vs* data: (a) $pCu \to \pi^- X$ ($\theta \approx 0$), the two curves correspond to highest and lowest proton momentum indicated (see [20] for references); (b) $\pi^-$ (top) and $\pi^+$ (bottom) spectra from a 10-cm thick lead target at $p_0$=8 GeV compared with data [22] and GEANT (FLUKA mode) [23] prediction.

intermediate energy range and of radionuclide production. To be usable in MARS, the CEM95 code is converted into double precision along with some other necessary modifications. Several examples of the CEM predictions compared with experimental data and results of several other models are given in Figs. 4 and 5. One can see that on the whole, the code reproduces quite well not only spectra of secondary nucleons but also excitation functions for the spallation yields, a much more *difficult* characteristic of nuclear reactions to be predicted by any theory, and is consistent with other well-known models [26].
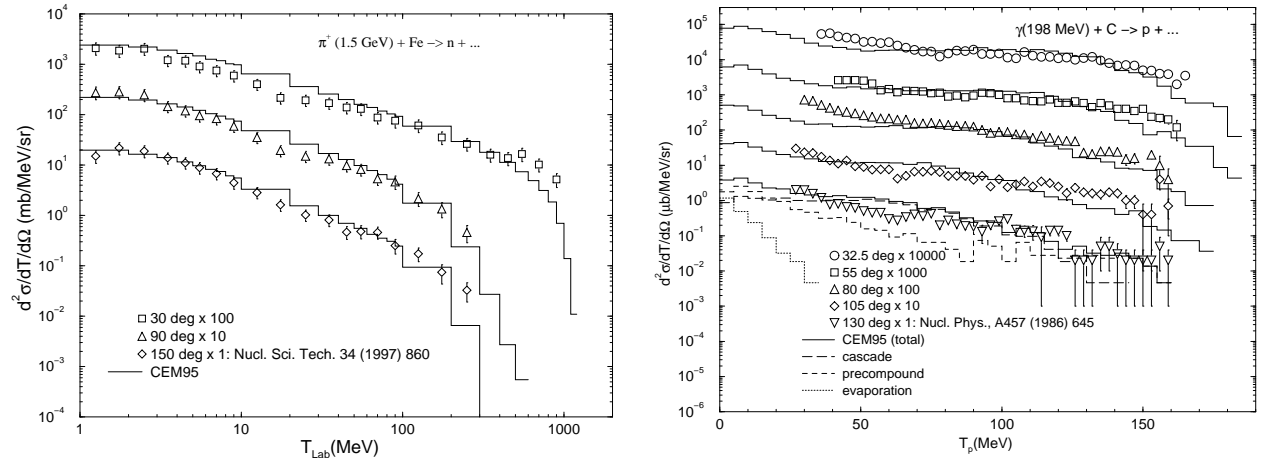


Figure 4. Double differential nucleon spectra as calculated with CEM95: (a) $\pi^+ Fe \to n + X$ for 1.5 GeV pions compared to data [24]; (b) $\gamma C \to p + X$ for 198 MeV photons compared to data [25].
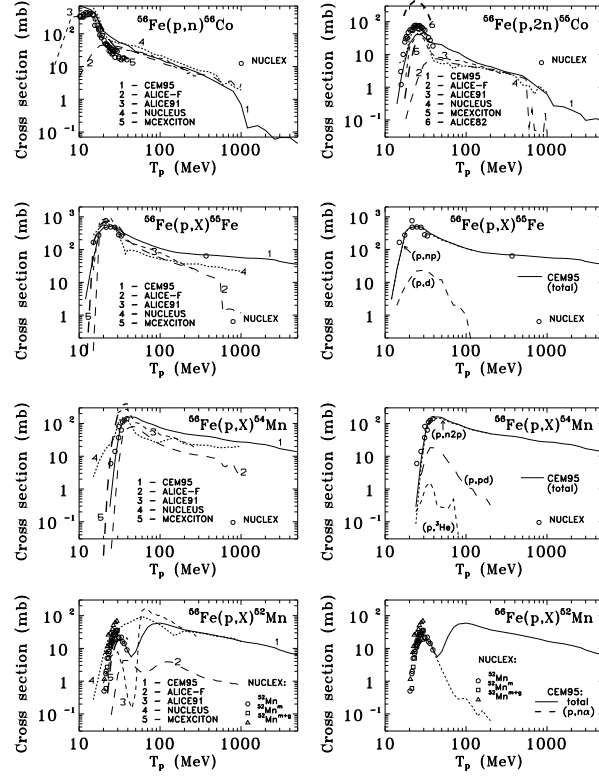
4

Figure 5. Excitation functions for the production of various radionuclides in $p +^{56}Fe$ spallation reactions *vs* proton kinetic energy calculated with CEM95 and compared with available experimental data and predictions of several other models. For details and references see [26].

**DPMJET for primary interactions.** The DPMJET-2.3/2.4 code [27] is implemented into MARS to sample the initial $hN$, $hA$, $AA$ and $\nu A$ interaction for 5 GeV<E<100 TeV. This provides—at least partially—features of a full exclusive event generation with all known particles in a final state. The DPMJET code has been proven to be consistent with collider and cosmic ray data in a multi-TeV energy region. The two-component Dual Parton Model is used with multiple soft chains and multiple minijets at each elementary interaction. Within this model the high energy projectile undergoes a multiple scattering process as formulated in the Glauber approach. Particle production is realized by the fragmentation of colorless parton-parton chains constructed from the quark content of the interacting hadrons. The code includes cascading of secondaries—suppressed by the formation time concept—within both target and projectile nucleus. The excitation energies of the remaining target– and projectile nuclei are calculated and simulation of subsequent nuclear evaporation is included in the model. The coupling of these new features to the MARS code is very CPU-time consuming and is used optionally only.

**Deuteron-nucleus collisions.** Deuteron interactions have little in common with the general picture of the interaction between complex nuclei because of the deuteron's relatively large size and small binding energy. Therefore a special model has been developed [28] and implemented into MARS. Deuteron-nucleus interactions are classified as elastic, dissociation, stripping, and full inelastic. In elastic interactions the deuteron emerges intact in the final state while the nucleus may be unchanged (coherent elastic) or have lost one nucleon (incoherent). Coherent elastic uses Glauber's treatment with some adjustments of the
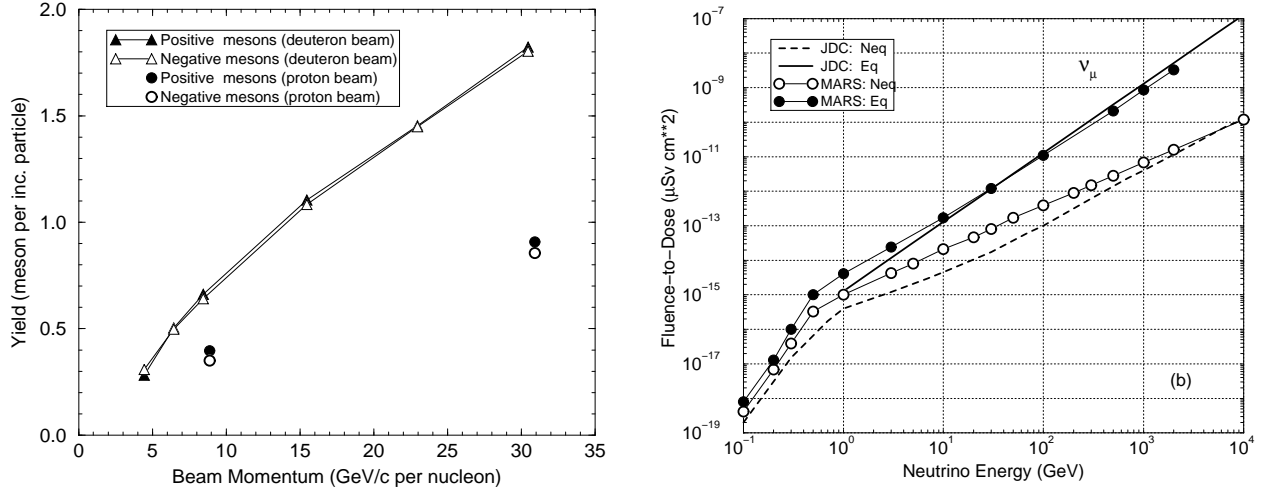
Figure 6. (a) $\pi, K$-meson yield from a gallium target for proton and deuteron beams calculated by MARS; (b) Dose equivalent in a bare (Neq) tissue phantom and in one embedded into an infinite medium (Eq) per unit neutrino fluence as calculated with MARS and estimated in [34].

parameters to fit experiment. Incoherent elastic scattering assumes a differential cross section to be twice that of the proton—using the prescription of [29]—and the nuclear parameters as for the coherent case. This is then multiplied by a deuteron– and a nucleon form factor as well as a Pauli suppression factor which hinders low momentum transfers. Exchange of a long range virtual photon may result in Coulomb dissociation whereby the deuteron splits into a proton and neutron. This is calculated using a Weiszacker-Williams approach for virtual photon emission. Dissociation may also result from (nuclear) elastic processes at relatively high momentum transfers. In stripping one nucleon undergoes an inelastic nuclear event while its partner continues without interaction. The total stripping probability is calculated based on the projected n–p separation as predicted by the deuteron wave function [30] and geometrical arguments. Deuterons dissociate as in [31] with full relativistic kinematics. Interaction with the nucleus by one of the partners proceeds within the standard MARS scheme. In full inelastic events both nucleons interact with the nucleus. The stripping routine provides the angular deflection and momentum of each nucleon after which both are allowed to interact as other MARS nucleons. As an example, a calculated $\pi, K$-meson yield out of a 3-cm radius gallium target 36-cm long in a 7.5-cm radius solenoid (B=20 T) is presented in Fig. 6(a) for proton and deuteron beams of equal momentum per nucleon.

**Neutrino-nucleus interactions.** Neutrinos from a high energy muon collider may cause a radiation problem at large distances from the source [32, 33]. Extraterrestrial neutrinos have also been examined as radiation hazards [34]. A special weighted neutrino interaction generator has been developed and incorporated into MARS. This model represents energy and angle of the particles—$e^\pm$, $\mu^\pm$, and hadrons—emanating from a simulated interaction. These particles, and the showers initiated by them, are then further processed by the MARS transport algorithms in the usual way. The four types of neutrinos are distinguished throughout: $\nu_\mu, \overline{\nu}_\mu, \nu_e, \overline{\nu}_e$. The model identifies the following types of neutrino interactions for $\nu_\mu$ ($\overline{\nu}_\mu$) and similarly for $\nu_e, (\overline{\nu}_e)$: $\nu_\mu N \rightarrow \mu^+ X, \nu_\mu N \rightarrow \nu_\mu X, \nu_\mu p \rightarrow \mu^+ n, \nu_\mu p \rightarrow \nu_\mu p, \nu_\mu n \rightarrow \nu_\mu n, \nu_\mu e^- \rightarrow \nu_\mu e^-, \nu_\mu e^- \rightarrow \nu_e \mu^-, \nu_\mu A \rightarrow \nu_\mu A$. The formulas for these processes as well as results of Monte Carlo simulations in general and in application to muon colliders in particular are described in [35]. Fig. 6(b) shows calculated dose in a 30-cm slab tissue-equivalent phantom irradiated with neutrinos of 100 MeV$< E_\nu <$10 TeV energy.

6

# 4 Stopped Hadrons and Muons

A very careful treatment is done in MARS of processes near and below the Coulomb barrier in hadron and muon transport (ionization absorption $vs$ nuclear interaction $vs$ decay).

**Pions.** A stopping $\pi^+$ decays into $\mu^+$ of 4.1 MeV plus a neutrino while a $\pi^-$ attaches to a nucleus (via the modified Fermi-Teller law). While cascading down the atomic energy levels, the pion is captured from a high orbit thus emitting only a few low energy photons which are neglected here. The hadronic interaction of the stopped $\pi^-$ is treated using the Cascade-Exciton Model [9] with a few modifications. When hydrogen is the target it is assumed there is a 60% probability to for charge exchange ($\pi^- p \rightarrow \pi^0 n$) whereupon the $\pi^0$ decays into two photons of 68.9 MeV each and the neutron acquires a small (0.4 MeV) kinetic energy. The remaining 40% of stopped $\pi^-$ in hydrogen interact via radiative capture: $\pi^- p \rightarrow n\gamma$. Here the photon acquires 129.4 MeV and the neutron 8.9 MeV kinetic energy. Other nuclides have a much smaller probability for radiative capture (1–2% which is taken into account in competition with CEM95). The photon energy is chosen from an empirical fit to experiment while the remainder is deposited as excitation energy.

**Muons.** A stopping $\mu^+$ always decays into $e\nu\overline{\nu}$ while a $\mu^-$ attaches itself to a nucleus. When a $\mu^-$ stops in a compound or mixture one first decides to which nucleus the $\mu^-$ attaches (modified Fermi-Teller law). Following attachment the muon may still decay as decided by comparing capture and decay lifetimes of which the latter is favored for light nuclei (Z≤11). A captured $\mu^-$ then cascades down to the ground state of the muonic atom emitting photons along with some Auger electrons, all of which is simulated using approximate fits to the atomic energy levels. In hydrogen muon capture always produces a 5.1 MeV neutron via inverse $\beta$-decay. In complex nuclei the giant dipole resonance plays a role and results in an 'evaporation'-type neutron spectrum with one or more resonances superimposed. This is illustrated in Fig. 7(a) which shows the neutron spectrum resulting from $\mu^-$ capture on oxygen. In addition smaller numbers of evaporation-type charged particles and photons may be emitted. Calculated with the above algorithms longitudinal dose distributions in a slab tissue-equivalent phantom are shown in Fig. 7(b) at the axis of 150 MeV proton and 75 MeV pion, muon and neutron beams striking the phantom.
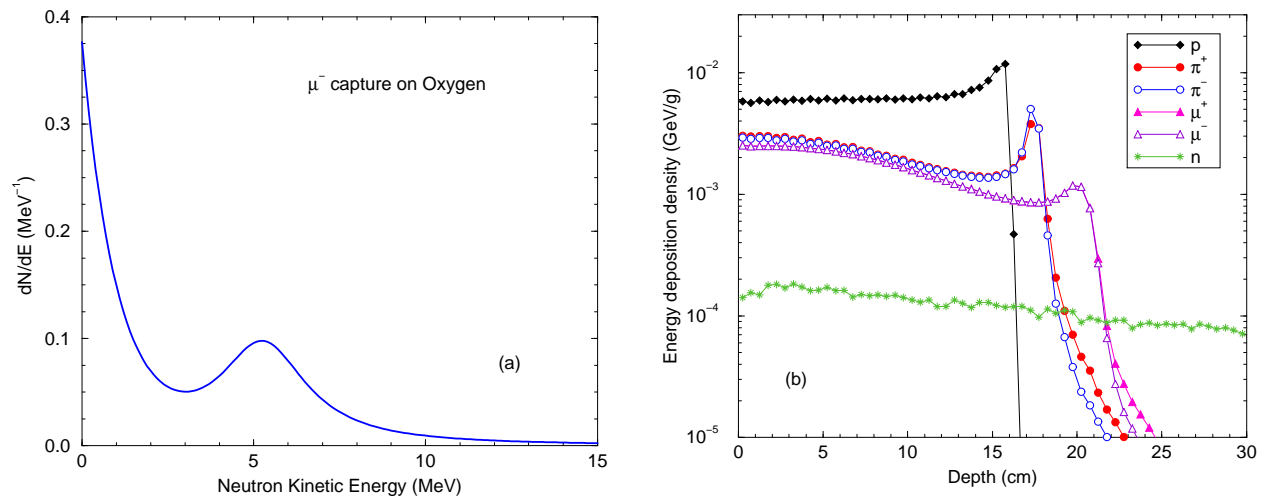


Figure 7. (a) Neutron spectrum generated in a $\mu^-$ capture on oxygen atom; (b) Axial absorbed dose in a tissue-equivalent phantom for a 150 MeV ($p$) and 75 MeV ($\pi^\pm, \mu^\pm, n$) 1×1 cm beams.

**Antiprotons.** Stopped $\overline{p}$ attach to nuclei in the same way as $\pi^-$ or $\mu^-$. Annihilation at rest is assumed to produce only pions, neglecting some of the rarer modes involving strange particles. Charges of produced pions are slightly skewed towards $\pi^-$ in view of the 'brought in' negative charge. Pion momenta are chosen from an inclusive distribution loosely based on experiment. The energy weighted distribution is normalized to twice the nucleon mass which predicts a multiplicity of 4.3—close to observation. In a complex nucleus the annihilation is treated as though it occurs on free nucleon except that each pion produced by the annihilation process is given a 50% probability to interact within the nucleus. This shortcut attempts to include—at least qualitatively—participation by the constituents nucleons.

For antiprotons in flight the annihilation cross section results in a larger cross section for $\overline{p}A$ vis-a-vis $pA$, especially for light nuclei at lower energies. Total cross sections for both $\overline{p}A$ and $pA$ are estimated on the basis of simple geometrical considerations and $\overline{p}p$, $\overline{p}n$ and $pp$,$pn$ cross sections. The ratio $\sigma_{\overline{p}A}/\sigma_{pA}$ is then applied to the more accurate $\sigma_{pA}$ used in MARS. Annihilation in flight uses the same inclusive pion distribution as at rest in the $\overline{p}$-nucleon rest frame after which the pions are Lorentz transformed back to the lab. Above about 0.1 GeV/c a small $\overline{p}p \rightarrow \overline{n}n$ component is included. For both mechanisms *nuclear* target effects are again approximated by allowing emerging particles to interact in the same nucleus or escape each with one half probability. There is also added a third component in which the $\overline{p}$ or $\overline{n}$ interact only quasi-elastically with the nucleons. These are simulated using conventional MARS algorithms exactly as for protons except that the fastest nucleon emerging (leading particle) from the collision is identified as its antiparticle.

# 5   Electromagnetic Processes.

**Unified treatment for hadrons and muons.** In muon and charged hadron electromagnetic processes, i.e., ionization and radiative collisions, with energy transfer $\varepsilon$ greater than a cutoff $\varepsilon_c$ are considered as discrete events involving production of $\delta$-electrons, $e^+e^-$-pairs, and bremsstrahlung [17]. The secondaries with $E > \varepsilon_c$ are followed explicitly. Energy losses with $\varepsilon < \varepsilon_c$ (so-called restricted losses) are considered as continuous. The restricted loss distribution is described by Vavilov's function with redefined parameters

$$\xi = Bs, \qquad B = 0.1536\frac{Z}{A\beta^2}$$
$$\kappa_n = \xi/\varepsilon_c, \qquad \beta_n^2 = \beta^2\varepsilon_c/\varepsilon_{\max} \tag{2}$$

where $Z$ and $A$ are the atomic and mass numbers of the absorber, $\beta c$ is the particle velocity, $\varepsilon_{\max}$ is the maximum energy transferred in a single collision, where the constant $B$ has dimensions $MeV \cdot g^{-1} \cdot cm^2$ so that, with the path-length $s$ expressed in g/cm$^2$, $\xi$ is in MeV. However, when $\kappa_n > 10$, the distribution becomes approximately Gaussian with mean

$$\bar{\Delta}_r = \alpha(\varepsilon < \varepsilon_c) \cdot s \tag{3}$$

and variance

$$\sigma_r^2 = \frac{\xi^2}{\kappa_n}(1 - \frac{\beta_n^2}{2}) \tag{4}$$

where $\alpha(\varepsilon < \varepsilon_c)$ is the mean restricted energy loss per unit length. The Gaussian approximation drastically simplifies the simulation. To simulate $\delta$-electron production at any step, one calculates $\varepsilon_\delta = \min(\varepsilon_G, \varepsilon_c)$ where $\varepsilon_G = \xi/10$. The restricted energy loss with $E < \varepsilon_\delta$ is then sampled from a Gaussian. The number of $\delta$-electrons with $E > \varepsilon_\delta$ is simulated using a Poisson distribution. The energy of each $\delta$-electron—if
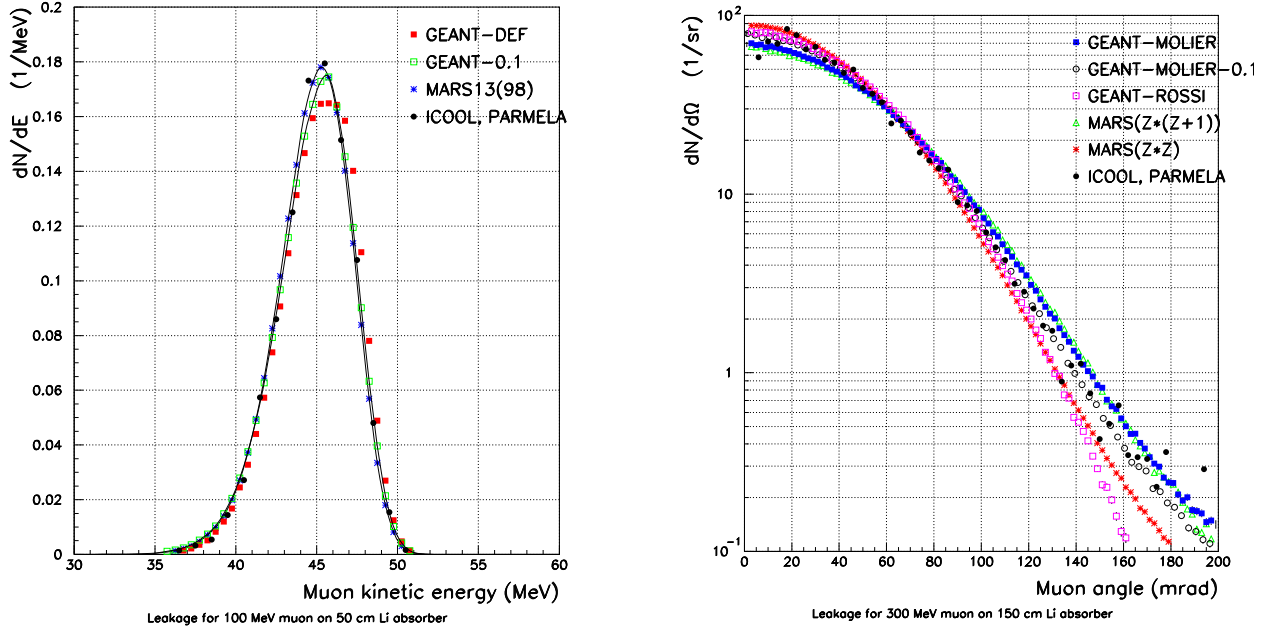
Figure 8. (a) Muon energy spectrum after a 50-cm lithium absorber for 100 MeV incident muons as calculated with MARS, GEANT [23] (in two modes) and ICOOL [36]; (b) Muon angular distribution after a 150-cm lithium absorber for 300 MeV incident muons as calculated with MARS, GEANT and ICOOL in a few modes.

any—is sampled from Bhabha's formula. Total energy loss of a particle is the sum of the $\delta$-electron energies and the restricted energy loss. Calculated energy spectrum and angular distributions of 100 and 300 MeV muons after lithium absorbers are shown in Fig. 8 in comparison with other calculations.

**Bremsstrahlung.** For muon bremsstrahlung, a precise but complex formalism [37] used previously as described in [17] has been replaced with a new simplified algorithm [38], which practically coincides with the exact formula. Total cross section and $dE/dx$ calculated by the two methods agree within 1%.

# 6  Other Enhancements

**Precise treatment of mixtures and compounds.** Precise treatment of individual elements in mixtures and compounds defined through the weight– or atomic fractions is done for all the electromagnetic and nuclear elastic and inelastic processes. Homogenization (averaging) thus becomes obsolete and is to be strongly discouraged. Atomic masses for 100 elements of the periodic table [10] and mean ionization energies and Sternheimer parameters [39, 40] are used by the code. All needed nuclear and electromagnetic cross sections and other parameters are calculated at the initialization stage for the specified composition of all materials present in the problem with a sample printout provided. Corresponding array sizes are adjusted according to energy. Up to 50 composite materials may be present in a given run.

**Automatic MARS-MCNP interface.** The code now includes an automatic interface of MARS materials to the MCNP code [41] for transport of low-energy neutrons and photons.

**List of particles.** MARS now includes $p, n, \pi^+, \pi^-, K^+, K^-, \mu^+, \mu^-, \gamma, e^-, e^+, \overline{p}, \pi^0, d, t, He^3, He^4, \nu$. In this version—for transport and output—$\overline{n}$ are included along with the neutrons, heavy fragments deposit their energy locally and short-lived hadrons and resonances are assumed to decay instantly into the appro-
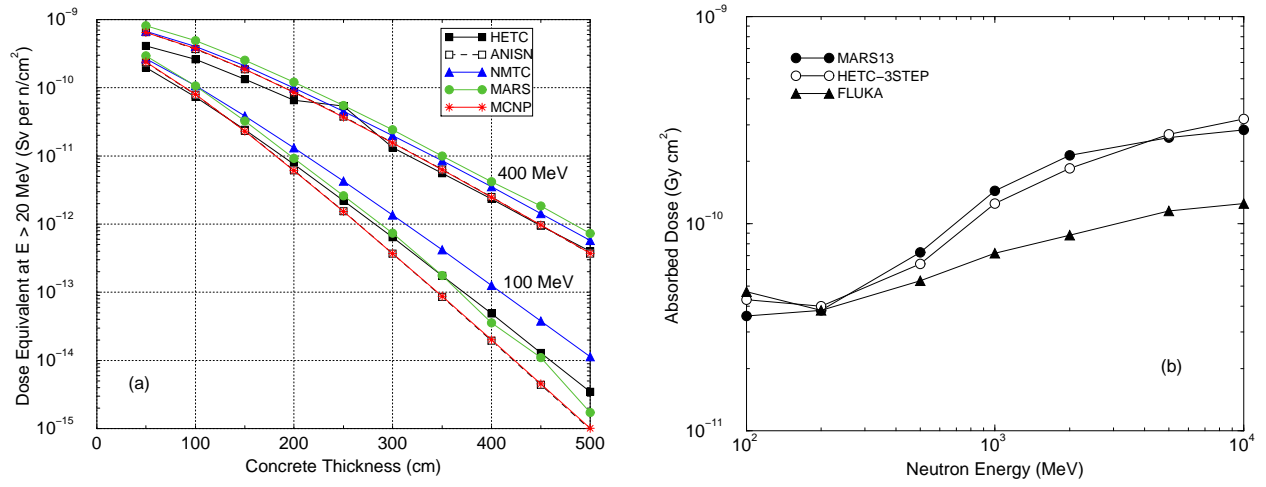
9

Figure 9. (a) Dose equivalent due to neutrons (E>20 MeV) in a thick concrete absorber irradiated with 100 and 400 MeV neutron beams as calculated with HETC, ANISN, NMTC, MARS and MCNP codes; (b) Absorbed dose per unit neutron fluence at 1-cm depth of a slab tissue-equivalent phantom *vs* neutron energy calculated with the MARS, HETC-3STEP and FLUKA codes.

priate particles which are then followed by the standard MARS algorithms.

**Geometry, visualization and histograming.** The Object-Oriented geometry engine and visualization module [3, 42] is further developed. Histograming and visualization capabilities of results, including a geometry-independent mesh-based scoring tool, are further extended. An interface to the ANSYS code [43] for thermal and stress analyses [3] for use in certain applications is slightly improved.

**Variance reduction.** Algorithms for splitting and Russian roulette at $hA$ vertices and in particle transport are further improved. For 'deep penetration' problems in complex highly non-uniform geometries, algorithms for scoring probabilities rather than real particle crossings or interactions now take into account all possible processes for both stable and unstable particles and charged as well as neutral hadrons.

**Recent benchmarking** Fig. 9(a) shows results of a recent SATIF-4 benchmarking for attenuation of dose equivalent (E>20 MeV neutrons only) in a thick concrete absorber for parallel almost mono-energetic neutron beams [44] of 100 and 400 MeV. Results calculated with HETC, ANISN, NMTC, MCNP, and MARS agree quite well over six decades at 400 MeV. At 100 MeV wider discrepancies are observed. Another SATIF-4 benchmarking has been performed for a 30-cm thick tissue-equivalent phantom irradiated with parallel mono-energetic neutron beams of 0.1 to 10 GeV energy [45]. Fig. 9b shows MARS results rather close to those of HETC-3STEP.

# 7 Conclusions

The MARS code physics and scoring possibilities have been substantially extended. The code's reliability is confirmed by several contributions to the SATIF/SARE meetings as well as in several more recent applications where MARS predictions show very good agreement with data. The official MARS site on the World Wide Web is *http://www-ap.fnal.gov/MARS/* which contains information about the code, its users, and its uses. At this site one can also register as a user and download the code for various platforms.

# References

[1] *http://www-ap.fnal.gov/MARS/*.

[2] N. V. Mokhov, "The MARS Code System Users Guide, Version 13(95)", Fermilab–FN–628, 1995.

[3] O. E. Krivosheev and N. V. Mokhov, "New MARS and its Applications", Proc. of the Third Workshop on Simulating Accelerator Radiation Environments (SARE3), KEK Proceedings 97-5, June 1997, pp. 12-20; Fermilab–Conf–98/043, 1998.

[4] Y. Nakane et al., "Intercomparison of Neutron Transmission Benchmark Analyses for Iron and Concrete Shields in Low, Intermediate and High Energy Proton Accelerator Facilities", OECD Proc. of the Third Specialists Meeting on Shielding Aspects of Accelerators, Targets and Irradiation Facilities (SATIF3 ), Tohoku Univ., Sendai, Japan, May 1997, pp. 151-182.

[5] H. Hirayama, "Intercomparison of the Medium-Energy Neutron Attenuation in Iron and Concrete", see [4], pp. 185-195.

[6] T. Suzuki et al., "Comparison Between Soil Benchmark Experiment and MARS Calculation", see [3], pp. 277-283; KEK Preprint 97-15, May 1997.

[7] S. G. Mashnik and A. J. Sierk, "Improved Cascade-Exciton Model of Nuclear Reactions", Proc. of the Fourth Workshop on Simulating Accelerator Radiation Environments (SARE4), Knoxville, TN, September 14-16, 1998.

[8] K. K. Gudima, S. G. Mashnik, and V. D. Toneev, "Cascade-Exciton Model of Nuclear Reactions", Nucl. Phys., **A401**, p. 329, 1983.

[9] S. G. Mashnik, "User Manual for the Code CEM95", JINR, Dubna, 1995; OECD Nuclear Energy Agency Data Bank, Paris, France, 1995; *http://www.nea.fr/abs/html/iaea1247.html*; RSIC-PSR-357, Oak Ridge, 1995.

[10] C. Caso et al., "Review of Particle Physics", Eur. Phys. J., **C3**, 1998.

[11] L. Montanet et al., "Review of Particle Properties", Phys. Rev., **D50**, No. 3, 1994.

[12] J. P. Burq et al., Nucl. Phys., **B217**, p. 285-335, 1983.

[13] V. S. Barashenkov, "Cross Sections of Interaction of Particles and Nuclei with Nuclei", JINR, Dubna, 1993.

[14] V. S. Barashenkov and A. Polanski, "Electronic Guide for Nuclear Cross Sections", JINR Communications E2-94-417, Dubna, 1994.

[15] G. D. Alkhazov et al., Phys. Rep., **42C**, p. 89, 1978.

[16] V. V. Burov, V. K. Lukianov and Yu. S. Pol, JINR P4-9556, Dubna, 1976.

[17] N. V. Mokhov and S. I. Striganov, "Simulation of Backgrounds in Detectors and Energy Deposition in Superconducting Magnets at $\mu^+\mu^-$ Colliders", in *Proceedings of the 9th Advanced ICFA Beam Dynamics Workshop: Beam Dynamics and Technology Issues for $\mu^+\mu^-$ Colliders*, Montauk, NY, October 15–20, 1995; also Fermilab–Conf–96/011 (1996).

[18] R. E. Prael and H. Lichtenstein, "User Guide to LCS: The LAHET Code System", LANL report LA-UR-89-3014, 1989.

[19] B. S. Sychev, "Approximation of the differential cross-section of nucleon-nuclei elastic scattering in the energy range above 10 MeV", *Vesti Akademii Nauk BSSR, Seriya Fiziko-energeticheckikh Nauk*, No. 4, Minsk, pp.13-16 (1986).

[20] N. V. Mokhov and S. I. Striganov, "Model for Pion Production in Proton-Nucleus Interactions", Proc. of the Workshop on Physics at the First Muon Collider, Fermilab, November 1997, AIP Conf. Proc. No. 435, pp. 453-459; Fermilab–Conf–98/053, 1998.

[21] T. Eichten et al., Nucl. Phys., **B44**, p. 333, 1972.

[22] M. F. Audus et al., Nuovo Cimento, **A46**, p. 502, 1966.

[23] *http://wwwinfo.cern.ch/asdoc/geant-html3/geantall.html*.

[24] T. Nakamoto, K. Ishibashi, N. Matsufuji, N. Shigyo, K. Maehata, H. Arima, S. Meigo, H. Takada, S. Chiba, and M. Numajiri, "Experimental Neutron-Production Double-Differential Cross Section for the Nuclear Reaction by 1.5-GeV $\pi^+$ Meson Incident on Iron", J. Nucl. Sci. and Technology, **34**, No. 8, pp. 860-862, 1997.

[25] M. Anghinolfi et al., Nucl. Phys., **A457**, pp. 645-656, 1986.

[26] S. G. Mashnik, A. J. Sierk, O. Bersillon, and T. Gabriel, "Cascade-Exciton Model Detailed Analysis of Proton Spallation at Energies from 10 MeV to 5 GeV", LA-UR-97-2905, Los Alamos, 1997; *http://t2.lanl.gov/publications/publications.html*.

[27] J. Ranft, *Phys. Rev.*, **D51**, 64, 1995; Gran Sasso report INFN/AE-97/45, 1997.

[28] N. V. Mokhov and A. Van Ginneken, in preparation.

[29] G. Belletini et al., Nucl. Phys., **79**, p. 609, 1966.

[30] L. Hulthen *Encyclopedia of Physics*, **39**, Springer Verlag, Berlin, 1957.

[31] R. Serber, Phys. Rev., **72**, p. 1008, 1947.

[32] B. J. King, private communication, 1996.

[33] N. V. Mokhov and A. Van Ginneken, "Muon Collider Neutrino Radiation", presented at Muon Collider Collaboration meeting, Orcas Island, VA, May 1997.

[34] J. D. Cossairt, N. L. Grossman, and E. T. Marshall, "Assessment of Dose Equivalent Due to Neutrinos", Health Physics, **73**, pp. 894-898, 1997.

[35] N. V. Mokhov and A. Van Ginneken, "Neutrino Induced Radiation at Muon Colliders", in preparation.

[36] R. Fernow, "ICOOL: Fortran Program to Simulate Muon Ionization Cooling", BNL, 1998, *http://pubweb.bnl.gov/people/fernow/readme.html*.

[37] Yu. M. Andreev and E. V. Bugaev, Izv. Akad. Nauk SSSR, Ser. Fiz., **42**, p. 1475, 1978.

[38] Yu. M. Andreev and E. V. Bugaev, Phys. Rev., **D55**. p. 1233, 1997.

[39] "Stopping Powers for Electrons and Positrons", ICRU Report No. 37, 1984.

[40] R. M. Sternheimer et al., "The Density Effect for the Ionization Loss of Charged Particles in Various Substances", Atomic Data and Nucl. Data Tables, **30**, p. 261, 1984.

[41] J. F. Briesmeister, editor, "MCNP - A General Monte Carlo N-Particle Transport Code". Version 4A. Pub. LA–12625–M, LANL, 1993.

[42] O. Krivosheev and N. Mokhov, "OO Geometry Engine for Monte-Carlo Simulation", *Proc. of Radiation Protection and Shielding Topical Meeting*, p. 487, No. Falmouths MA, 1996.

[43] Swanson Analysis Systems, *Inc*.,"ANSYS (Revision 5.1)", SASI/DN-P511:51, Houston, USA, 1994.

[44] H. Hirayama, "Intercomparison of the Medium-Energy Neutron Attenuation in Iron and Concrete", Fourth Specialists Meeting on Shielding Aspects of Accelerators, Targets and Irradiation Facilities (SATIF-4), Knoxville, TN, September 17-18, 1998.

[45] N. Yoshizawa, "Comparison of Computer Code Calculations for the ICRU Slab Phantom", Fourth Specialists Meeting on Shielding Aspects of Accelerators, Targets and Irradiation Facilities (SATIF-4), Knoxville, TN, September 17-18, 1998.